Pergamon

Geochimica et Cosmochimica Acta, Vol. 68, No. 1, pp. 183–194, 2004

0016-7037/04 \$30.00 + .00

doi:10.1016/S0016-7037(03)00368-5

Petrography and oxygen isotopic compositions in refractory inclusions from CO chondrites

SHOICHI ITOH,[1,*] HIDEYASU KOJIMA,[2] and HISAYOSHI YURIMOTO[1]

[1]Department of Earth and Planetary Sciences, Tokyo Institute of Technology, Meguro, Tokyo 152-8551 Japan
[2]National institute of Polar Research, Kaga, Itabashi, Tokyo 173-8515 Japan

(*Received January* 10, 2003; *accepted in revised form May* 5, 2003)

Abstract—Fine-grained Ca-Al-rich inclusions (FGIs) in Yamato-81020 (CO3.0) and Kainsaz (CO3.1–CO3.2) chondrites have been studied by secondary ion mass spectrometry. The FGIs from Yamato-81020 consist of aggregates of hibonite, spinel, melilite, anorthite, diopside and olivine grains with no petrographic evidence of alteration. In contrast, the FGIs from Kainsaz commonly contain alteration products such as nepheline. From replacement textures and chemical compositions of altered and unaltered FGIs, we conclude that the alteration products formed by decomposition of melilite and anorthite. All phases in the Yamato-81020 FGIs are enriched in ^{16}O, with $\delta^{17,\,18}O = \sim -40‰$ except for one FGI that experienced melting. Oxygen isotopic compositions of melilite, anorthite, some spinel and diopside in Kainsaz FGIs changed from $\delta^{17,\,18}O = \sim -40‰$ toward 0‰ by aqueous alteration. Alteration products in FGIs are depleted in ^{16}O relative to primary phases, with $\delta^{17,\,18}O = \sim 0‰$. These results show that FGIs in CO chondrites commonly had ^{16}O-rich compositions in the solar nebula. The original ^{16}O-rich FGIs were modified to ^{16}O-poor compositions during aqueous alteration in the parent body. *Copyright © 2004 Elsevier Ltd*

1. INTRODUCTION

Refractory inclusions have been classified as Ca-Al-rich inclusions (CAIs) based on their petrographic and chemical characteristics (e.g., MacPherson et al., 1988). Previous O-isotope studies of coarse-grained CAIs (CGIs) from various types of carbonaceous chondrites have shown that oxygen isotopic compositions of CGI minerals are generally distributed along the carbonaceous chondrite anhydrous minerals (CCAM) line on a three-O isotope diagram (e.g., Clayton, 1993; Clayton and Mayeda, 1999). The O-isotopic distributions indicate that the spinel and Al-Ti-pyroxene (fassaite) in CGIs usually have $\delta^{17,\,18}O = \sim -40‰$, whereas melilite and anorthite in CGIs mostly have $\delta^{17,\,18}O = \sim 0‰$. A recent study of the O-isotope microdistribution within and among minerals (Yurimoto et al., 1998) shows that multiple heating events in different O isotopic environments are essential to CGI formation.

Previous petrographic studies of chondrites revealed that various type of chondrites (ordinary chondrite [OC], enstatite chondrite [EC] and carbonaceous chondrite [CC]) usually contain FGIs in different abundances (e.g., Grossman et al., 1988). Previous oxygen isotopic studies of FGIs from different petrologic classes of chondrite (OC, EC, CI, CV, CM, CO, CH, CK, CR) usually reported ^{16}O-rich characteristics of spinel and diopside in FGIs (e.g., Huss et al., 1995; McKeegan et al., 1998; Hiyagon and Hashimoto, 1999; Sahijpal et al., 1999; Sakai and Yurimoto, 1999; Guan et al., 2000; Itoh et al., 2000; Fagan et al., 2001; Krot et al., 2001; Wasson et al., 2001; Yurimoto et al., 2001; Krot et al., 2002). However, the origin of the ^{16}O-poor nature of FGI minerals remained unclear because of the strong alteration effects for such small grains of FGIs compared with those of CGIs (e.g., Fagan et al., 2002), i.e., it remained unknown whether ^{16}O-poor FGI minerals were originally ^{16}O-rich or ^{16}O-poor.

CO chondrites contain many FGIs with sizes ranging from a few tens to hundreds of micrometers across (Tomeoka et al., 1992; Kojima et al., 1995; Russell et al., 1998). Many FGIs from CO3.0 meteorites (Y-81020, Colony) appear to be unaltered and retain their original characteristics. In contrast, effects of aqueous alteration gradually appear in FGIs with increasing petrographic subtype of host CO chondrite (Kojima et al., 1995; Wasson et al., 2001). The alteration appears to have resulted in the replacement of melilite by a fine-grained mixture of nepheline and other phases such as andradite and hedenbergite. With increasing petrographic subtypes (>3.5), spinel grains in FGIs become more Fe-rich, reaching ~50–60 mol.% hercynite probably due to redistribution of FeO by thermal metamorphism (McSween, 1977a; Itoh and Tomeoka, 2003). Kojima et al. (1995) proposed that such alteration and metamorphism occurred in the parent body based on the observation that the degree of alteration and metamorphic effects observed in FGIs increase with petrographic subtypes of the host. This inference is supported by hydrothermal experiments that show that the Na-rich minerals (e.g., nepheline) typical of secondary alteration products in CAIs can be formed by aqueous alteration of melilite with hydrothermal fluid (Nomura and Miyamoto, 1998).

Clayton and Mayeda (1999) suggested that the variation of bulk O-isotopic compositions in different petrologic subtypes (CO3.0–CO3.7) could be attributed to the variable degree of aqueous alteration. In our preliminary O-isotopic work (Itoh et al., 2000) we reported about the alteration effect for the minerals except melilite of various petrographic FGI-types from different metamorphic grade CO3 chondrites. Other previous work has addressed changes in mineralogy and textures (McSween, 1977a; Chizmadia et al., 2002) and O-isotopic composition of a single phase (Wasson et al., 2001) over a large range of CO subtypes. In this study, we focus on the mineralogy and O-isotopic compositions near the onset of the metamorphic sequence to determine: (1) the original O-isotopic systematics of CO FGIs and (2) relationships between textural alteration

* Author to whom correspondence should be addressed (sitoh@geo.titech.ac.jp).

Table 1. Representative compositions in Yamato-81020 inclusion.

Type:	Spinel-melilite-pyroxene					Spinel-melilite-pyroxene			Melilite-rich inclusion		
Inclusion:	Y20-9					Y20-8			Y20-3		
Mineral:	Diopside		Spinel	Melilite		Diopside	Spinel	Melilite	Melilite	Diopside	Perovskite
No. in Fig. 1:	1	2	3	4	5				1	2	
Na_2O	n.d.	n.d.	n.d.	n.d.	n.d.	n.d.	n.d.	n.d.	n.d.	n.d.	n.d.
MgO	18.1	18.7	27.1	2.3	2.3	17.5	27.9	6.1	1.3	17.1	n.d.
Al_2O_3	0.6	0.8	69.4	31.2	30.8	2.8	71.2	24.3	34.1	3.6	n.d.
SiO_2	53.9	55.4	n.d.	24.6	25.3	52.2	n.d.	29.2	23.5	52.5	n.d.
CaO	26.1	25.4	n.d.	41.5	41.2	25.1	n.d.	40.3	40.5	25.5	40.3
TiO_2	n.d.	n.d.	0.7	n.d.	n.d.	n.d.	n.d.	n.d.	n.d.	n.d.	55.4
FeO	n.d.	n.d.	n.d.	n.d.	n.d.	0.5	n.d.	n.d.	n.d.	0.6	0.5
Cr_2O_3	n.d.	n.d.	n.d.	n.d.	n.d.	n.d.	n.d.	n.d.	n.d.	n.d.	n.d.
Total:	98.7	100.4	97.2	99.6	99.6	98.0	99.1	99.9	99.5	99.3	96.2
Na	n.d.	n.d.	n.d.	n.d.	n.d.	n.d.	n.d.	n.d.	n.d.	n.d.	n.d.
Mg	0.99	1.00	0.98	0.16	0.16	0.96	0.99	0.41	0.09	0.93	n.d.
Al	0.03	0.03	1.99	1.69	1.67	0.12	2.01	1.30	1.84	0.15	n.d.
Si	1.97	1.99	n.d.	1.13	1.16	1.92	n.d.	1.33	1.08	1.91	n.d.
Ca	1.02	0.98	n.d.	2.05	2.03	0.99	n.d.	1.97	1.99	1.00	1.02
Ti	n.d.	n.d.	0.01	n.d.	n.d.	n.d.	n.d.	n.d.	n.d.	n.d.	0.98
Fe	n.d.	n.d.	n.d.	n.d.	n.d.	0.01	n.d.	n.d.	n.d.	0.02	0.01
Cr	n.d.	n.d.	n.d.	n.d.	n.d.	n.d.	n.d.	n.d.	n.d.	n.d.	n.d.
O	6.00	6.00	4.00	7.00	8.00	6.00	4.00	7.00	7.00	6.00	3.00
Cations	4.01	4.00	2.99	5.03	5.01	4.00	3.00	5.01	5.00	4.01	2.02
$\delta^{17}O$	–49.0	–41.5	–46.8	–45.0	–40.3	–45.7	–46.0	–40.0	−44.2	−42.5	n.m.
$\delta^{18}O$	–43.4	–43.0	–43.9	–39.0	–38.3	–40.8	–47.7	–38.9	−33.8	−37.8	n.m.
$\sigma_{mean}(^{17}O)$	2.2	2.1	2.6	2.3	2.2	2.1	2.8	2.4	2.2	2.3	n.m.
$\sigma_{mean}(^{18}O)$	1.2	1.1	1.2	1.0	1.0	1.8	1.0	1.3	1.1	1.1	n.m.

Ti-Al-Di = Ti-Al-rich diopside. Al-Di = Al-rich diopside. r-Di = diopside from rim of the inclusion. No. of Fig. 1: the numbers correspond to SIMS analyses position in Fig. 1. n.d. = not detected. n.m. = not measured due to small size. σ_{mean}: standard deviation of the mean determined by statistical variation of secondary ion intensities corresponding to precisions for a series of measurements.

and oxygen isotopic evolution in the CO chondrites. We discuss the oxygen isotopic signatures of FGIs from CO chondrites based on relationships between petrologic properties and chemical compositions for individual crystals in FGIs from two CO chondrites of different petrologic subtype, Y-81020 (CO3.0) and Kainsaz (CO3.1–CO3.2) (subtypes from Sears et al., 1991; Kojima et al., 1995; Shibata, 1996; Chizmadia et al., 2002).

2. EXPERIMENTAL PROCEDURES

2.1. Scanning Electron Microscopy and X-Ray Analysis

Polished thin sections of Yamato-81020 (#61-1) on loan from National Institute of Polar Research and of Kainsaz (TTK1) were used in this study. They were examined with a petrographic microscope and with a JEOL JSM-5310LV scanning electron microscope equipped with an Oxford LINK-ISIS energy dispersive X-ray spectrometer (SEM-EDS) at the Tokyo Institute of Technology (TiTech). Backscattered electron images and quantitative analyses were obtained with this system. X-ray intensities for major elements were collected at 15 keV with a beam current of 1 nA for quantitative analyses. The measurement time for each point was 100 seconds. ZAF corrections were applied to the X-ray data to obtain quantitative values.

2.2. Secondary Ion Mass Spectrometry (SIMS)

In situ oxygen isotopic analysis was performed with the TiTech CAMECA ims 1270 SIMS instrument. The primary ion beam was mass-filtered positive $^{133}Cs^+$ ions accelerated to 20 keV and the beam spot size was adjusted to 3–5 μm in diameter. Negative secondary ions of the $^{16}O_{tail}$, ^{16}O, ^{17}O, ^{16}OH and ^{18}O were analyzed at a mass resolution power of > 6000, sufficient to eliminate the hydride interference on the ^{17}O peak. Other analytical conditions and data calibration methods have been described elsewhere (Yurimoto et al., 1998). The reported precision of each analysis was determined by secondary ion stability (Tables 1–3). The overall analytical accuracy is estimated as ±5‰ (1σ). Since the FGI minerals are fine-grained, we carefully evaluated overlapping of the primary beam among mineral phases by scanning electron microscope after SIMS analysis. Data affected by beam overlap on multiple phases show intermediate O isotopic values.

3. RESULTS AND DISCUSSION

3.1. Petrography and Oxygen Isotope Characteristics

3.1.1. Yamato-81020, 61-1(Y20): Pristine Fine-Grained CAIs

About 37 mm^2 of thin section #61-1 of Y-81020 CO3 chondrite have been carefully observed by SEM-EDS in this study. In this area, 169 FGIs, ~4.6 particles/mm^2, were iden-

Type:	Hibonite-pyroxene-olivine				Spinel-anorthite-pyroxene				Spinel-anorthite-pyroxene					
Inclusion:	Y20-7				Y20-6				Y20-1					
Mineral:	Ti-Al-Di	Al-Di	Hibonite	Olivine	Spinel	Diopside	Anorthite	Al-Di	Diopside		Al-Di	r-Di	Spinel	Anorthite
No. in Fig. 1:	1	2	3	4	1	2	3		1	2		3	4	5
Na_2O	n.d.	n.d.	n.d.	n.d.	n.d.	n.d.	n.d.	n.d.	n.d.	n.d.	n.d.	n.d.	n.d.	0.2
MgO	8.2	10.2	0.6	55.5	27.1	17.1	0.3	7.0	13.8	15.4	7.0	16.4	27.1	0.2
Al_2O_3	23.7	19.0	90.8	n.d.	71.9	8.5	37.2	24.0	12.9	12.3	22.7	5.7	72.3	36.3
SiO_2	39.0	42.3	n.d.	42.8	n.d.	49.0	42.0	35.8	47.2	46.8	34.4	51.7	n.d.	43.8
CaO	26.5	26.6	8.8	n.d.	n.d.	23.3	19.9	23.8	25.2	23.6	25.2	24.0	n.d.	20.0
TiO_2	1.4	0.4	1.3	n.d.	n.d.	0.9	n.d.	9.6	1.7	2.2	10.7	0.4	n.d.	n.d.
FeO	0.4	n.d.	0.2	1.7	0.3	0.4	n.d.	0.3	n.d.	n.d.	n.d.	1.8	0.5	n.d.
Cr_2O_3	n.d.	n.d.	n.d.	n.d.	n.d.	n.d.	n.d.	n.d.	n.d.	n.d.	0.2	0.4	0.8	n.d.
Total:	99.2	98.5	101.6	100.0	99.2	99.1	99.4	100.5	100.8	100.3	100.2	100.5	100.7	100.5
Na	n.d.	n.d.	n.d.	n.d.	n.d.	n.d.	n.d.	n.d.	n.d.	n.d.	n.d.	n.d.	n.d.	0.01
Mg	0.45	0.56	0.09	1.91	0.96	0.92	0.02	0.38	0.74	0.83	0.39	0.88	0.95	0.02
Al	1.03	0.83	11.76	n.d.	2.0	0.37	2.04	1.03	0.54	0.52	0.99	0.24	2.01	1.97
Si	1.44	1.56	n.d.	0.99	n.d.	1.78	1.96	1.30	1.69	1.68	1.27	1.87	n.d.	2.02
Ca	1.04	1.05	1.04	n.d.	n.d.	0.91	1.00	0.93	0.97	0.91	1.00	0.93	n.d.	0.99
Ti	0.04	0.01	0.10	n.d.	n.d.	0.02	n.d.	0.26	0.05	0.06	0.30	0.01	n.d.	n.d.
Fe	0.01	n.d.	0.02	0.03	0.01	0.01	n.d.	0.01	n.d.	n.d.	n.d.	0.06	0.01	n.d.
Cr	n.d.	n.d.	n.d.	n.d.	n.d.	n.d.	n.d.	n.d.	n.d.	n.d.	0.01	0.01	0.02	n.d.
O	6.00	6.00	19.00	4.00	4.00	6.00	8.00	6.00	6.00	6.00	6.00	6.00	4.00	8.00
Cations	4.01	4.01	13.01	2.93	2.97	4.01	5.02	3.92	3.99	4.00	3.94	4.00	2.99	5.00
$\delta^{17}O$	−46.3	−41.9	−50.7	−36.7	−44.8	−39.7	−42.4	n.m.	−21.0	21.2	n.m.	−16.1	−38.0	−16.3
$\delta^{18}O$	−41.4	−44.3	−49.1	−39.5	−47.8	−39.9	−38.6	n.m.	−17.8	−17.2	n.m.	−14.1	−32.0	−15.1
$\sigma_{mean}(^{17}O)$	2.4	2.0	2.4	2.2	2.0	1.6	2.1	n.m.	2.4	2.2	n.m.	1.9	2.1	2.2
$\sigma_{mean}(^{18}O)$	0.9	1.2	1.1	1.0	1.3	1.3	1.3	n.m.	2.0	1.8	n.m.	1.6	1.2	1.8

tified. The FGIs from Yamato-81020 have a size range of 50–200 μm across (Fig. 1). Individual mineral grains are difficult to discern by optical microscope (i.e., categorized as FGIs; MacPherson et al., 1988). We analyzed chemical and oxygen isotopic compositions at the same points in each mineral (Table 1). All FGIs contain Fe-free spinel (FeO $<$ 0.1 wt.%; Table 1) and are free of alteration products such as nepheline, hedenbergite and andradite. All O-isotope ratios of these FGI minerals generally plot on the CCAM line and are enriched in ^{16}O, with $\delta^{17}O$, $^{18}O_{SMOW} = \sim -40‰$ (Fig. 2). Based on mineralogy, the FGIs have been classified into four groups: (1) spinel-melilite-pyroxene (Sp-Mel-Px) inclusions (73 particles; 43%), (2) melilite-rich inclusions (4 particles; 3%), (3) hibonite-pyroxene-olivine (Hib-Px-Ol) inclusions (2 particles; 1%) and (4) spinel-anorthite-pyroxene (Sp-An-Px) inclusions (90 particles; 53%). The characteristics of each FGI type are described below.

3.1.1.1. Spinel-melilite-pyroxene inclusions. Sp-Mel-Px inclusions (Fig. 1a) are irregularly-shaped with sizes up to 200 μm across. Sp-Mel-Px inclusions always have a core of spinel enclosed by a melilite layer completely surrounded by a diopside layer. This type of inclusion rarely contains hibonite and grossite grains enclosed by the melilite layer. Similar inclusions have been described previously in CO3 chondrites including Y-81020 in this study (Y-81020: Kojima et al., 1995; Colony: Russell et al., 1998, and Wasson et al., 2001). Rare Sp-Mel-Px inclusions contain an anorthite layer between the melilite and diopside layers. All phases from this type of inclusion are enriched in ^{16}O, with $\delta^{17,\,18}O_{SMOW} = \sim -40‰$ (Table 1).

3.1.1.2. Melilite-rich inclusions. Melilite-rich inclusions (Fig. 1b) are irregularly shaped with sizes up to 100 μm. Cavities are commonly observed in the melilite aggregates. Diopside crystals are present, but in contrast to the Sp-Mel-Px inclusions, diopside does not form continuous rims around the Mel-rich FGIs. Melilite grains are directly in contact with matrix. Melilite and diopside are enriched in ^{16}O, with $\delta^{17,\,18}O_{SMOW} = \sim -40‰$ (Table 1).

3.1.1.3. Hibonite-pyroxene-olivine inclusions. Hib-Px-Ol inclusions (Fig. 1c) are ellipse-shaped with sizes up to 100 μm. Porous texture is observed at the rim of Al-rich diopside. Similar inclusions, most with crystalline fassaite, have been previously described in CO3 and CM2 chondrites (Ireland et al., 1991; Tomeoka et al., 1992; Russell et al., 1998; Simon et al., 1998). All phases in the Hib-Px-Ol inclusion are enriched in ^{16}O, with $\delta^{17,\,18}O_{SMOW} = \sim -40‰$ (Table 1). Oxygen isotopic compositions in the olivine rim are enriched in ^{16}O (Table 1), similar to those of olivines in AOAs from the Allende CV3 chondrite and from the same thin section of Y-81020 CO3.0 chondrite used in this study (Hiyagon and Hashimoto, 1999; Imai and Yurimoto, 2001; Itoh et al., 2002). This olivine might be part of an accretionary rim.

Table 2. Representative compositions in Kainsaz Ca-Al-rich inclusions.

Type:	Spinel-Alteration-Pyroxene							Spinel-Alteration-Pyroxene					spinel-alteration-pyroxene			
Inclusion:	TK1-16							TK1-1					TK1-19			
Mineral:	Diopside		Spinel		Nepheline		Melilite	Spinel		Diopside	Al-Di	Perovskite	spinel	Al-Di	graftonite	
No. in Fig. 3	1	2	3	4	5	6	7									
Na_2O	n.d.	n.d.	n.d.	n.d.	19.9	19.8	n.d.	n.d.	0.6	n.d.	n.d.	n.d.	n.d.	n.d.	n.d.	n.d.
MgO	18.1	15.2	17.6	17.9	0.6	n.d.	1.7	16.1	19.3	17.9	13.8	3.6	25.7	5.7	n.d.	n.d.
Al_2O_3	0.6	8.6	67.0	67.2	35.9	34.3	32.0	62.6	66.8	0.8	21.1	5.6	69.9	25.5	n.d.	n.d.
SiO_2	53.9	49.4	n.d.	n.d.	40.7	41.8	24.2	n.d.	0.6	53.2	38.3	n.d.	n.d.	28.6	n.d.	n.d.
CaO	26.1	24.8	n.d.	n.d.	n.d.	0.7	39.9	2.3	0.2	25.6	21.1	23.3	n.d.	24.0	56.8	56.0
TiO_2	n.d.	n.d.	n.d.	n.d.	n.d.	n.d.	n.d.	n.d.	0.9	n.d.	2.3	51.8	0.6	17.1	n.d.	n.d.
FeO	n.d.	1.3	13.4	14.1	1.7	2.3	n.d.	15.8	11.4	0.6	1.9	13.7	2.3	n.d.	n.d.	n.d.
Cr_2O_3	n.d.	n.d.	n.d.	n.d.	n.d.	n.d.	n.d.	1.2	n.d.	n.d.	n.d.	n.d.	n.d.	n.d.	n.d.	n.d.
P_2O_5	n.d.	1.3	n.d.	n.d.	n.d.	n.d.	n.d.	n.d.	n.d.	n.d.	n.d.	n.d.	n.d.	n.d.	43.8	42.9
SO_3	n.d.	n.d.	n.d.	n.d.	n.d.	n.d.	n.d.	n.d.	n.d.	n.d.	n.d.	n.d.	n.d.	n.d.	n.d.	n.d.
K_2O	n.d.	n.d.	n.d.	n.d.	n.d.	n.d.	n.d.	n.d.	n.d.	n.d.	n.d.	n.d.	n.d.	n.d.	n.d.	n.d.
ZnO	n.d.	n.d.	n.d.	n.d.	n.d.	n.d.	n.d.	n.d.	n.d.	n.d.	n.d.	n.d.	n.d.	n.d.	n.d.	n.d.
Total:	98.7	100.6	98.0	99.1	98.8	98.8	97.8	98.0	99.9	98.1	98.5	98.0	98.5	100.9	100.6	99.0
Na	n.d.	n.d.	n.d.	n.d.	0.93	0.92	n.d.	n.d.	0.03	n.d.	n.d.	n.d.	n.d.	n.d.	n.d.	n.d.
Mg	0.99	0.83	0.67	0.68	0.02	n.d.	0.12	0.63	0.72	0.98	0.76	0.13	0.93	0.31	n.d.	n.d.
Al	0.03	0.37	2.03	2.01	1.02	0.97	1.76	1.94	1.97	0.03	0.92	0.15	2.00	1.11	n.d.	n.d.
Si	1.97	1.80	n.d.	n.d.	0.98	1.01	1.13	n.d.	0.02	1.97	1.42	n.d.	n.d.	1.06	n.d.	n.d.
Ca	1.02	0.97	n.d.	n.d.	n.d.	0.02	1.99	0.07	0.01	1.01	0.84	0.58	n.d.	0.95	3.17	3.18
Ti	n.d.	n.d.	n.d.	n.d.	n.d.	n.d.	n.d.	n.d.	0.02	n.d.	0.07	0.90	0.01	0.47	n.d.	n.d.
Fe	n.d.	0.04	0.29	0.30	0.03	0.05	n.d.	0.35	0.24	0.02	0.06	0.27	0.05	n.d.	n.d.	n.d.
Cr	n.d.	n.d.	n.d.	n.d.	n.d.	n.d.	n.d.	0.03	n.d.	n.d.	n.d.	n.d.	n.d.	n.d.	n.d.	n.d.
P	n.d.	n.d.	n.d.	n.d.	n.d.	n.d.	n.d.	n.d.	n.d.	n.d.	n.d.	n.d.	n.d.	n.d.	1.93	1.93
S	n.d.	n.d.	n.d.	n.d.	n.d.	n.d.	n.d.	n.d.	n.d.	n.d.	n.d.	n.d.	n.d.	n.d.	n.d.	n.d.
K	n.d.	n.d.	n.d.	n.d.	n.d.	n.d.	n.d.	n.d.	n.d.	n.d.	n.d.	n.d.	n.d.	n.d.	n.d.	n.d.
Zn	n.d.	n.d.	n.d.	n.d.	n.d.	n.d.	n.d.	n.d.	n.d.	n.d.	n.d.	n.d.	n.d.	n.d.	n.d.	n.d.
O	6.00	6.00	4.00	4.00	4.00	4.00	7.00	4.00	4.00	6.00	6.00	3.00	4.00	6.00	8.00	8.00
Cations	4.01	4.01	2.99	2.99	2.98	2.97	5.00	3.02	3.00	4.01	4.07	2.03	2.99	3.90	5.10	5.11
$\delta^{17}O$	−34.9	−27.8	−42.6	−45.4	−9.0	−2.4	−4.0	−40.4	−41.2	−39.8	−41.2*	n.m.	−40.1	−31.7	5.2	−1.1
$\delta^{18}O$	−30.3	−22.1	−41.6	−41.6	−3.9	−1.2	0.6	−40.5	−33.8	−34.6	−33.8*	n.m.	−40.4	−30.3	12.3	11.2
$\sigma_{mean}(^{17}O)$	2.3	2.4	2.3	2.5	2.2	2.1	2.3	2.4	2.3	2.1	2.3*	n.m.	2.2	2.1	2.1	2.3
$\sigma_{mean}(^{18}O)$	1.2	1.3	1.0	1.0	0.9	1.0	1.0	1.0	1.0	1.2	1.1*	n.m.	0.9	1.1	1.2	1.1

Al-Di = Al-rich diopside. p- = primary area. a- = alteration area. c- = core. r- = rim. No. of Fig. 3: the numbers correspond to SIMS analyses position in Fig. 3. n.d. = not detected. n. m. = not measured due to small size. σ_{mean}: standard deviation of the mean determined by statistical variation of secondary ion intensities corresponding to precisions for a series of measurements. * overlapping spinel (20%) and Al-rich diopside (80%). # overlapping spinel (50%) and hibonite (50%); the reported data means one spot analysis. ′ overlapping of anorthite (50%) and alteration mineral (50%). ″ overlapping of Al-rich diopside (50%) and alteration mineral (50%).

3.1.1.4. Spinel-anorthite-pyroxene inclusions. Two textural subtypes of Sp-An-Px inclusions were recognized. One type (e.g., Y20-6; Fig. 1d) is characterized by irregular shapes and consists of aggregates of grains, suggesting condensation products from vapor to solid. This type of FGI shows a concentric structure with a core of spinel enclosed by anorthite and surrounded by diopside. The FGIs often contain small Al-rich diopside grains (<5 μm) enclosed by anorthite. Previous studies have proposed that the anorthite was produced by the reaction between precondensed melilite and high temperature nebula gas (Lin and Kimura, 1998). Similar textures have been previously described in Al-rich inclusions in amoeboid olivine aggregates (AOAs) from CV (McSween, 1977b; Kornacki and Wood, 1984; Hashimoto and Grossman, 1987; Komatsu et al., 2001) and from CO chondrites, including Y-81020 in this study (McSween, 1977a; Chizmadia et al., 2002; Itoh et al., 2002). All phases of Y20-6 FGI are enriched in ^{16}O, with $\delta^{17,\,18}O_{SMOW} = \sim -40‰$ (Table 1).

The other type of Sp-An-Px inclusions (e.g., Y20-1; Fig. 1e) has an igneous texture indicating crystallization from a melt. The FGI shows a poikilitic texture, with spinel enclosed in subhedral anorthite and subhedral diopside. The FGIs commonly contain small (<5 μm) Al-rich diopside grains enclosed by diopside. The bulk chemical compositions (MgO, 12.4 wt.%; Al_2O_3, 22.2 wt.%; SiO_2, 42.5 wt.%; CaO, 21.2 wt.%; TiO_2, 1.5 wt.%; Cr_2O_3, 0.4 wt.%; FeO, 0.6 wt.%) correspond to the type-C CAI field of Stolper's diagram (Stolper, 1982; Wark, 1987). The petrographic texture is consistent with crystallization of the type-C melt. This type of FGI might have originated from melting of Sp-An-Px inclusions without igneous texture. All phases of Y20-1 except spinel grains are relatively depleted in ^{16}O, but spinel is enriched in ^{16}O, with $\delta^{17,\,18}O_{SMOW} = \sim -40‰$ (Table 1). The O-isotopic distribution and igneous texture suggest that spinel is a relict phase and the other phases (Al-diopside, diopside and anorthite) crystallized from melt with $\delta^{17,\,18}O_{SMOW} = \sim -15‰$.

3.1.2. Kainsaz (TTK-1): Altered Fine-Grained CAIs

Forty CAIs categorized as FGIs have been observed in an area of ~9 mm^2 in the TTK1 thin section. The abundance of

Type:	spinel-alteration-pyroxene			spinel-alteration				pyroxene-alteration		melilite-alteration-pyroxene						hibonite-pyroxene		
Inclusion:	TK1-30			TK1-9				TK1-29		TK1-12						TK1-6		
Mineral:	spinel	diopside	hibonite	spinel	hibonite	ilmenite	alteration	diopside	alteration	p-melilite	p-anorthite	p-Al-Di	a-melilite	alteration	a-Al-Di	hibonite	c-Al-Di	r-Al-Di
No. in Fig. 3				1	1		2	1	2	1	2	3	4	5	6	1	2	3
Na_2O	n.d.	n.d.	n.d.	n.d.	n.d.	n.d.	5.9	n.d.	17.2	n.d.	n.d.	2.1	n.d.	14.4	n.d.	n.d.	n.d.	n.d.
MgO	13.9	18.7	2.4	7.4	2.4	0.8	3.2	19.4	n.d.	3.7	0.3	10.8	2.8	n.d.	13.3	n.d.	9.3	16.2
Al_2O_3	63.9	2.5	82.5	60.6	83.6	1.1	37.8	0.6	35.9	28.5	35.7	17.5	30.4	36.3	12.0	88.2	26.0	12.5
SiO_2	n.d.	54.8	n.d.	n.d.	n.d.	0.5	29.1	53.9	43.7	26.8	41.5	42.3	25.0	43.2	47.5	n.d.	40.1	46.0
CaO	2.6	24.0	8.6	n.d.	n.d.	n.d.	2.9	24.3	0.5	39.7	20.1	22.7	38.4	4.0	26.6	8.5	24.6	21.3
TiO_2	n.d.	n.d.	4.1	n.d.	n.d.	n.d.	n.d.	n.d.	n.d.	n.d.	n.d.	5.2	n.d.	n.d.	1.7	1.6	1.7	n.d.
FeO	17.2	1.4	0.6	n.d.	8.3	5.1	14.6	n.d.	1.1	0.6	n.d.	n.d.	1.2	0.9	n.d.	0.8	0.8	2.2
Cr_2O_3	0.5	n.d.	n.d.	n.d.	4.4	50.5	n.d.	n.d.	n.d.	n.d.	n.d.	n.d.	n.d.	n.d.	n.d.	n.d.	n.d.	n.d.
P_2O_5	n.d.	n.d.	n.d.	29.3	1.0	39.2	n.d.	n.d.	n.d.	n.d.	n.d.	n.d.	n.d.	n.d.	n.d.	n.d.	n.d.	n.d.
SO_3	n.d.	n.d.	n.d.	n.d.	n.d.	n.d.	2.5	n.d.	n.d.	n.d.	n.d.	n.d.	n.d.	n.d.	n.d.	n.d.	n.d.	n.d.
K_2O	n.d.	n.d.	n.d.	n.d.	n.d.	n.d.	1.7	n.d.	n.d.	n.d.	n.d.	n.d.	n.d.	n.d.	n.d.	n.d.	n.d.	n.d.
ZnO	n.d.	n.d.	n.d.	n.d.	n.d.	n.d.	0.6	n.d.	n.d.	n.d.	n.d.	n.d.	n.d.	n.d.	n.d.	n.d.	n.d.	n.d.
Total:	98.1	101.4	98.2	97.3	99.7	97.2	98.2	98.2	98.4	99.3	97.6	100.6	97.8	98.8	101.2	99.1	102.5	98.2
Na	n.d.	n.d.	n.d.	n.d.	n.d.	n.d.		n.d.		n.d.	n.d.	0.15	n.d.		n.d.	n.d.	n.d.	n.d.
Mg	0.55	0.99	0.38	0.31	0.38	0.03		1.06		0.25	0.02	0.58	0.19		0.71	n.d.	0.49	0.89
Al	1.99	0.10	11.21	2.00	11.15	0.03		0.03		1.54	2.00	0.75	1.67		0.51	11.74	1.08	0.54
Si	n.d.	1.95	1.01	n.d.	n.d.	0.01		1.97		1.23	1.98	1.53	1.17		1.70	n.d.	1.42	1.69
Ca	0.07	0.91	0.38	n.d.	n.d.	n.d.		0.95		1.95	1.03	0.88	1.92		1.02	1.03	0.93	0.84
Ti	n.d.	n.d.	0.06	n.d.	n.d.	n.d.		n.d.		n.d.	n.d.	0.14	n.d.		0.05	0.14	0.05	n.d.
Fe	0.38	0.04	n.d.	n.d.	1.01	0.14		n.d.		0.02	n.d.	n.d.	0.05		n.d.	0.08	0.02	0.07
Cr	0.01	n.d.	n.d.	n.d.	0.38	0.96		n.d.		n.d.	n.d.	n.d.	n.d.		n.d.	n.d.	n.d.	n.d.
P	n.d.	n.d.	n.d.	0.69	0.06	0.83		n.d.		n.d.	n.d.	n.d.	n.d.		n.d.	n.d.	n.d.	n.d.
S	n.d.	n.d.	n.d.	n.d.	n.d.	n.d.		n.d.		n.d.	n.d.	n.d.	n.d.		n.d.	n.d.	n.d.	n.d.
K	n.d.	n.d.	n.d.	n.d.	n.d.	n.d.		n.d.		n.d.	n.d.	n.d.	n.d.		n.d.	n.d.	n.d.	n.d.
Zn	n.d.	n.d.	n.d.	n.d.	n.d.	n.d.		n.d.		n.d.	n.d.	n.d.	n.d.		n.d.	n.d.	n.d.	n.d.
O	4.00	6.00	19.00	4.00	19.00	3.00		6.00		7.00	8.00	6.00	7.00		6.00	19.00	6.00	6.00
Cations	3.00	4.00	13.04	3.00	12.98	2.00		4.01		4.99	5.03	4.03	5.00		3.99	12.99	3.99	4.03
$\delta^{17}O$	−32.9	−35.6	−36.3	−31.8#	−31.8#	n.m.	1.5	−42.0	0.4	−28.1	−17.2	−35.6	−5.3	2.0′	−12.4″	−40.7	−34.1	−30.0
$\delta^{18}O$	−31.9	−36.7	−43.3	−27.4#	−27.4#	n.m.	2.4	−33.9	7.3	−20.0	−17.4	−35.6	−0.9	1.7′	−8.1″	−39.4	−36.6	−25.5
$\sigma_{mean}(^{17})$	2.5	1.8	2.3	2.2#	2.2#	n.m.	2.1	2.1	2.0	2.3	2.4	2.4	2.6	2.5′	2.2″	2.3	2.3	2.3
$\sigma_{mean}(^{18}O)$	1.3	0.9	1.2	1.0#	1.0#	n.m.	0.9	1.2	1.2	1.3	1.4	1.3	1.5	1.1′	1.4″	1.1	1.4	1.1

FGIs in Kainsaz is ~4.4 particles/mm^2. They have a size range of 20–400 μm across. Typical textures are shown in Figures 3 and 4. All of the Kainsaz FGIs contain alteration products such as nepheline. The FGIs have been classified into five groups: (1) spinel-alteration-pyroxene (Sp-Alt-Px) inclusions, including one extremely altered FGI, TK1-3 (22 particles; 55%); (2) spinel-alteration (Sp-Alt) inclusions (3 particles; 8%); (3) pyroxene-alteration (Px-Alt) inclusions (12 particles; 30%); (4) melilite-alteration-pyroxene inclusions (Mel-Alt-Px) (2 particles; 5%); and (5) hibonite-pyroxene inclusions (Hib-Px) (1 particle; 3%). All groups correspond to those in Y-81020 if alteration phases result from the decomposition of melilite and anorthite. We analyzed chemical and oxygen isotopic compositions at the same points in each mineral (Tables 2 and 3). Oxygen isotopic analyses of minerals from each of these FGI types generally plot on the CCAM line (Fig. 5). The characteristics of each FGI type and the heavily altered FGI are described below.

3.1.2.1. Spinel-alteration-pyroxene inclusions. Sp-Alt-Px inclusions (Fig. 3a) are compact objects consisting of layered aggregates ~10–20 μm across, with fine spinel grains (5–75 mol.% hercynite) enclosing 1–5 μm perovskite, hibonite laths, grossite and ilmenite grains. Aggregates of fine melilite enclosed by nepheline layers were rarely observed. From the inside to outward, the spinel grains are surrounded by a 2–10-μm layer of diopside (Al_2O_3 = ~5 wt.%). A thin alteration layer (2 to ~10 μm) is present between the spinel core and diopside layer. The alteration layer consists of nepheline or unidentified Na-Ca-Al-rich silicates. The diopside layer contains troilite grains. Throughout the inclusions are veins of Fe-rich material that may be due to terrestrial weathering. Spinel and diopside are generally enriched in ^{16}O, with $\delta^{17,\,18}O_{SMOW}$ = ~−40‰ (Table 2). Graftonite ([Fe, Mn, Ca]$_3$[PO$_4$]$_2$), as is typical of alteration products, occurs in masses of fine grains surrounding nodules of spinel and diopside, and is depleted in ^{16}O relative to spinel and diopside, with $\delta^{17,\,18}O_{SMOW}$ = ~0‰. Melilite also has $\delta^{17,\,18}O_{SMOW}$ = ~0‰. The ^{16}O-poor characteristics of melilite are similar to those from Ornans FGIs (Wasson et al., 2001). Comparing the texture and O isotopic compositions between Kainsaz and Y-81020, this inclusion type corresponds to Sp-Mel-Px and/or Sp-An-Px inclusions of Y-81020, in which melilite and anorthite have been altered to nepheline.

Table 3. Representative compositions in TK1-3 Kainsaz Ca-Al-rich inclusions

Mineral:	Spinel						Diopside		Hibonite	Grossite
No. Fig. 4	sp#A1	sp#A2	sp#A3	sp#A4	sp#B5	sp#B6	di#1	di#2		
Na_2O	n.d.	n.d.	1.1	n.d.	n.d.	n.d.	0.4	n.d.	n.d.	n.d.
MgO	6.9	7.4	7.2	6.5	10.2	11.0	17.0	10.9	4.1	1.0
Al_2O_3	61.0	58.2	59.6	59.3	65.5	64.7	2.5	14.8	80.6	73.8
SiO_2	n.d.	n.d.	0.6	0.4	0.5	0.5	52.5	42.4	0.7	0.4
CaO	n.d.	n.d.	n.d.	n.d.	n.d.	n.d.	25.2	23.8	8.2	21.3
TiO_2	n.d.	n.d.	n.d.	n.d.	n.d.	n.d.	0.5	4.2	5.4	n.d.
Cr_2O_3	n.d.	n.d.	n.d.	n.d.	n.d.	n.d.	0.5	1.1	n.d.	n.d.
FeO	32.2	32.6	31.9	33.5	23.7	22.7	1.1	1.4	0.7	1.1
ZnO	n.d.	n.d.	n.d.	n.d.	1.2	1.4	n.d.	n.d.	n.d.	n.d.
Total:	100.1	98.2	100.4	99.7	101.1	100.3	99.7	98.6	99.7	97.6
Na	n.d.	n.d.	0.06	n.d.	n.d.	n.d.	0.03	n.d.	n.d.	n.d.
Mg	0.28	0.31	0.30	0.27	0.40	0.43	0.92	0.60	0.69	0.07
Al	1.98	1.94	1.94	1.95	2.03	2.01	0.11	0.65	10.78	3.89
Si	n.d.	n.d.	0.02	0.01	0.01	0.01	1.92	1.58	0.08	0.02
Ca	n.d.	n.d.	n.d.	n.d.	n.d.	n.d.	0.99	0.95	1.00	1.02
Ti	n.d.	n.d.	n.d.	n.d.	n.d.	n.d.	0.01	0.12	0.46	n.d.
Cr	n.d.	n.d.	n.d.	n.d.	n.d.	n.d.	0.02	0.03	n.d.	n.d.
Fe	0.74	0.77	0.74	0.78	0.52	0.50	0.03	0.04	0.07	0.04
Zn	n.d.	n.d.	n.d.	n.d.	0.02	0.03	n.d.	n.d.	n.d.	n.d.
O	4.00	4.00	4.00	4.00	4.00	4.00	6.00	6.00	19.00	7.00
Cations	3.00	3.02	3.06	3.01	2.99	2.98	4.03	3.97	13.08	5.04
$\delta^{17}O$	0.1	−3.2	−0.2	−1.3	−41.5	−42.2	−10.9	−12.2	n. m.	n. m.
$\delta^{18}O$	1.1	1.8	1.1	1.9	−42.9	−37.6	−3.0	−6.8	n. m.	n. m.
$\sigma_{mean}(^{17}O)$	2.5	2.4	2.0	2.2	2.8	2.2	2.4	1.6	n. m.	n. m.
$\sigma_{mean}(^{18}O)$	1.1	1.1	0.9	1.1	1.1	1.0	1.0	0.8	n. m.	n. m.
$FeAl_2O_4$%	73	71	71	74	56	54				

No. of Fig. 4: the numbers correspond to SIMS analyses position in Fig. 4. n.d. = not detected. n.m. = not measured due to small size. σ_{mean}: standard deviation of the mean determined by statistical variation of secondary ion intensities corresponding to precisions for a series of measurements.

3.1.2.2. Spinel-alteration inclusions. Sp-Alt inclusions (Figs. 3b and 3c) are irregularly-shaped. The cores of these inclusions consist of fine-grained spinel (40–70 mol.% hercynite) that often encloses perovskite, ilmenite, ulvöspinel and laths of hibonite. The spinel grains are surrounded by an altered zone consisting of a fine-grained mixture of nepheline, diopside, and troilite (Fig. 3c). In unaltered spinel ± hibonite–bearing FGIs from Y-81020, this domain adjacent to spinel consists of melilite and anorthite (Fig. 1a). This texture suggests that the altered layer formed from decomposition of melilite and anorthite. In addition, high hercynite contents of spinel indicate that the degree of alteration of this inclusion is relatively high. These observations are consistent with previous reports which showed similar type inclusions tend to have high hercynite contents of spinel (Tomeoka et al., 1992; Kojima et al., 1995; Russell et al., 1998). The area of mixed spinel and hibonite shows $\delta^{17,\,18}O_{SMOW} = \sim\!-30$‰ (Table 2). In contrast, the alteration phase has an oxygen isotopic composition of $\delta^{17,18}O_{SMOW} = \sim\!0$‰ (Table 2). Comparing the texture and O-isotopic compositions between FGIs in Kainsaz and Y-81020, this inclusion type corresponds to Sp-Mel-Px inclusions of Y-81020 in which the original melilite was altered.

3.1.2.3. Pyroxene-alteration inclusions. Px-Alt inclusions (Fig. 3d) are irregularly-shaped and are divided into diopside and alteration layer. The diopside layer often rims the inclusions of this type. The alteration layer is a mixture of nepheline, unidentified Na-Al-Si-rich silicates, diopside, Al-rich diopside ($Al_2O_3 = \sim\!20$ wt.%, $TiO_2 = \sim\!10$ wt.%) and FeS. Some samples of this inclusion type contain spinel grains (<2 μm) with corroded texture, which is similar in texture to the spinel-alteration-pyroxene inclusions. The corroded texture of the small spinel grains suggests that spinel has been partially decomposed during alteration. The diopside is enriched in ^{16}O, with $\delta^{17,\,18}O_{SMOW} = \sim\!-40$‰ (Table 2), whereas the Na-Al-Si-rich silicates and nepheline have oxygen isotopic compositions of $\delta^{17,\,18}O_{SMOW} = \sim\!0$‰ (Table 2). This inclusion type might correspond to spinel-anorthite-pyroxene and spinel-melilite-pyroxene inclusions from Y-81020 in which spinel, melilite and anorthite were changed to unidentified Na-Al-Si-rich silicates and nepheline.

3.1.2.4. Melilite–alteration-pyroxene inclusions. Mel-Alt-Px (Figs. 3e–3g) inclusions are irregularly-shaped. These FGIs consist of small melilite grains that are enclosed by nepheline and rare anorthite, surrounded by Al-rich diopside ($Al_2O_3 = \sim\!13$ to $\sim\!18$ wt.%; Table 2). Al-rich diopside grains are in contact with matrix and also occur in the interior of these FGIs. Parts of the TK1-12 Mel-Alt-Px FGI are heavily altered and other parts are not (Figs. 3e–3g). In the area with abundant primary phases (Fig. 3f), the melilite and Al-rich diopside have O-isotopic compositions of about $\delta^{17,\,18}O_{SMOW} = \sim\!-30$‰, whereas anorthite is relatively depleted in ^{16}O, with $\delta^{17,\,18}O_{SMOW} = \sim\!-15$‰ (Table 2). In the area with abundant alteration products (Fig. 3g), much of the melilite and anorthite has been converted to nepheline. Melilite in

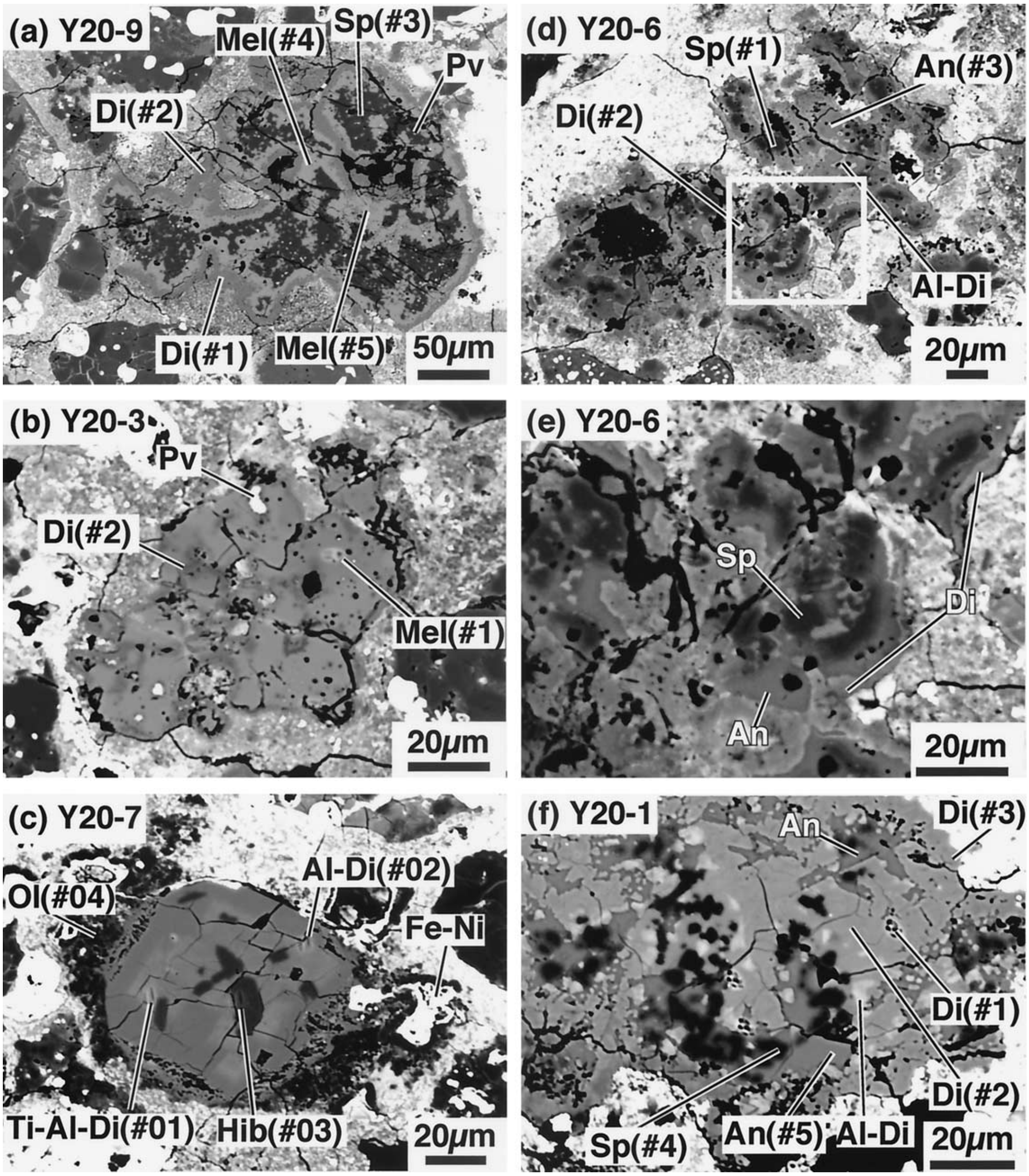

Fig. 1. Representative back-scattered electron (BSE) images of several CAIs in Y-81020. The numbers in the figure correspond with analyses of chemical and O-isotopic compositions reported in Table 1. Mineral abbreviations: Mel, melilite; Pv, perovskite; Sp, spinel; Di, diopside; Al-Di, Al-rich diopside; An, anorthite; Hib, hibonite; Ol, olivine. (a) Compact Sp-Mel-Px inclusion, Y20-9, 150 μm across. The CAI consists of a core of fine spinel aggregates (FeO < 0.1 wt.%) surrounded by melilite ($Åk_{5-17}$). The rim consists of diopside ($Al_2O_3 = \sim 0.5$ wt.%). The CAIs are compact but many pores are observed in the sp-mel core. Perovskite grains 1 to 5 μm in size occur in the core. (b) Melilite-rich inclusion, Y20-3, 100 μm across. The CAI is irregularly shaped, and mostly composed of melilite ($Åk_{2-10}$) that encloses small patches of perovskite and diopside. (c) Hib-Px-Ol inclusion, Y20-7, 80 μm across. The CAI is ellipse shaped, and is composed of laths of hibonite (TiO_2 ~2–3 wt.%) that are enclosed by Ti-Al-rich diopside ($TiO_2 = \sim 1.4$ wt.%, $Al_2O_3 = \sim 24$ wt.%) and Al-rich diopside ($TiO_2 = \sim 0.4$ wt.%, $Al_2O_3 = \sim 19$ wt.%). Aggregates of olivine grains (~5 μm) partly enclose the diopside core. The diopside has sector zoning of Ti. The lighter areas of diopside have high Ti contents. (d) An irregularly shaped Sp-An-Px inclusion, Y20-6, 150 μm across. The CAI consists of a core of fine spinel aggregates (FeO < 0.1 wt.%) and Al-rich diopside ($Al_2O_3 = \sim 30$ wt.%) enclosed by anorthite. A rim of diopside encloses the CAI. ($Al_2O_3 = \sim 18$ wt.%). (e) High magnification BSE image corresponds to the white square area of Figure 1d. All minerals indicate the anhedral texture. (f) An irregularly shaped compact Sp-An-Px inclusion, Y20-1, 150 μm across. The CAI is composed of subhedral diopside ($Al_2O_3 = \sim 13$ wt.%), small patches of Al-rich diopside (Al_2O_3 ~22 wt.%) and subhedral anorthite enclosing spinel aggregates (FeO = ~0.5 wt.%). Some of the anorthite and diopside grains have euhedral angular crystal margins. Small rounded perovskite grains are often observed. They are rimmed by 2–10 μm crystals of diopside ($Al_2O_3 = \sim 6$ wt.%). SIMS analysis spots appear in diopside as sputtered craters.

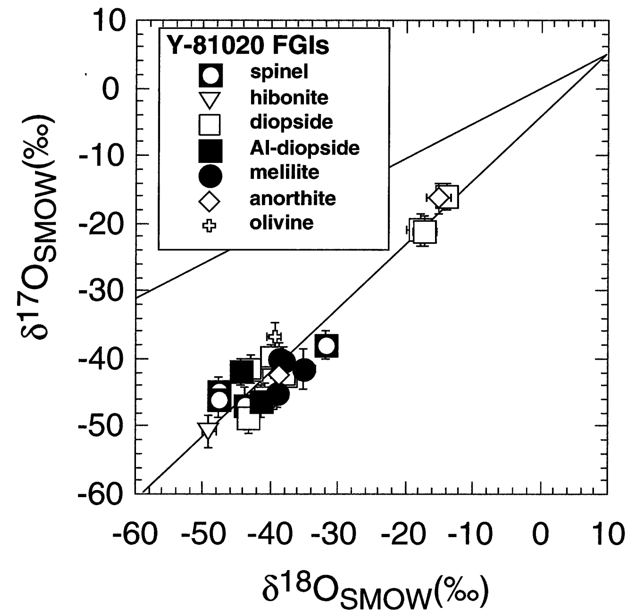

Fig. 2. Oxygen isotopic compositions of minerals from FGIs in Y-81020. Analyses from all the FGI types of Y-81020 are plotted. All phases in FGIs from Y-81020 have O-isotopic compositions ($\delta^{17,\ 18}$O = ~ -40 to -50‰) except for anorthite and diopside in Y20-1 FGI.

this area is depleted in ^{16}O, with $\delta^{17,\ 18}O_{SMOW} = \sim 0$‰ (Table 2). Oxygen isotopic analyses of alteration minerals mixed with adjacent Al-rich diopside and anorthite indicate that the alteration products are depleted in ^{16}O relative to the primary phases (Table 2). The correlation between melilite isotopic composition and alteration texture within a FGI indicates that ^{16}O-depletion of FGI melilite in Kainsaz occurred during alteration.

3.1.2.5. Hibonite-pyroxene inclusion. Only one Hib-Px inclusion (Fig. 3h) has been observed in Kainsaz TTK1. This inclusion is ellipse-shaped and appears similar in texture to the Y20-7 FGI in Y-81020 (Fig. 1c). The Al-rich diopside in the core has higher Al_2O_3 and TiO_2 contents (Al_2O_3 = 25–30 wt.%; $TiO_2 = \sim 1.5$ wt.%) than that at the rim ($Al_2O_3 = \sim 12$ wt.%, TiO_2 is not detected; Table 2). The rim of this inclusion has an anhedral shape. The rim of diopside contains small round (~ 2 μm) Na-Ca-Al-Fe-rich silicates. All of the primary minerals in TK1-6 are enriched in ^{16}O with $\delta^{17,\ 18}O_{SMOW}$ = ~ -40‰ (Table 2). The distribution of oxygen isotopic composition is similar to that found in hibonite-pyroxene-olivine inclusion, Y20-7.

3.1.2.6. Heavily altered inclusion. TK1-3 is classified as a Sp-Alt-Px inclusion (Figs. 4a–4c) but it appears to be more heavily altered than the other Kainsaz FGIs and is described separately here. The spinel in this inclusion has the highest FeO content (~ 75 mol.% hercynite) of any spinel in the Kainsaz FGIs (Table 3). The spinel core is divided into a porous part (Sp#A) and a smooth part (Sp#B) (Fig. 4). The FeO content of spinel in the porous part (~ 70 mol.% hercynite) is higher than that in the smooth part (~ 50 mol.% hercynite; Table 3). ZnO contents are ~ 1 wt.% in the smooth part and are below detection in the porous part (Table 3). The two parts have contrasting O-isotopic compositions; the smooth part has $\delta^{17,\ 18}O_{SMOW} = \sim -40$‰, and the porous part has $\delta^{17,\ 18}O_{SMOW} = \sim 0$‰. The diopside is porous and has ^{16}O-poor compositions with $\delta^{17,\ 18}O_{SMOW} = \sim -10$‰, in contrast to those of other inclusions in Y-81020 and Kainsaz. The only ^{16}O-poor spinel and diopside identified in this study are porous grains in this heavily altered FGI.

3.2. Comparison of Alteration of CAIs in Y-81020 and Kainsaz

3.2.1. Petrologic and isotopic evidence of thermal metamorphism and aqueous alteration

CAIs in Y-81020 consist of primary high-temperature phases such as hibonite, melilite, spinel, Al-rich diopside, diopside and anorthite, while most CAIs in Kainsaz contain major amounts of alteration products that probably replaced primary melilite and anorthite. Therefore, CAIs from Y-81020 show pristine textures and compositions of FGIs, whereas FGIs from Kainsaz show the effects of alteration. These petrographic and chemical descriptions are consistent with those of previous work on CO chondrites (Kojima et al., 1995; Chizmadia et al., 2002). Because the previous studies (Kojima et al., 1995; Chizmadia et al., 2002) suggest that the characteristics result from aqueous alteration in the parent body and evidence of aqueous alteration in the CO parent body has been observed in dark inclusions (Itoh and Tomeoka, 2003), it is plausible that the alteration observed in this study is due to the same processes. The degree of alteration varies among individual CAIs even within thin sections of meteorites of the same petrographic classification. Some of the heterogeneity of alteration may be due to a parent body brecciation effect. However, degree of alteration varies within a single FGI (Fig. 3e). Therefore, alteration progressed heterogeneously on a mm-scale in the CO parent body and alteration effects varied in different locations and/or at different times in this parent body.

Aqueous alteration of FGIs begins with ^{16}O-depletion of originally ^{16}O-rich melilite and anorthite. Melilite-alteration-pyroxene inclusions from Kainsaz in this study (Fig. 3e) and in Wasson et al. (2001) experienced O-isotopic exchange. After O-isotopic exchange, the melilite and anorthite reacted with aqueous fluid to form alteration products, mainly nepheline (Figs. 3a, 3b, 3d, and 3e). Secondary phases have ^{16}O-poor isotopic compositions near the SMOW value, consistent with the variation in bulk compositions of CO chondrites with increasing petrographic subtype (Clayton and Mayeda, 1999).

FGIs from Kainsaz commonly contain diopside having a porous texture or interfingered alteration phases along grain boundaries (Figs. 3e and 3h). Such diopside has not been observed in the Y-81020 FGIs. Porous diopside is poorer in Al_2O_3 than massive diopside but it retains its ^{16}O-rich nature (Table 2). Our results indicate that the process of aqueous alteration changes textures and chemical compositions of diopside without significant O-isotopic exchange in this stage.

Hercynite contents of spinel grains range from 5 to 75 mol.% in Kainsaz FGIs, compared to $<$ 2 mol.% in spinel from Y-81020 (Fig. 6). The high hercynite contents are inconsistent with equilibrium condensation from a solar gas at high temperatures (e.g., Grossman, 1972). Kojima et al. (1995) and Russell et al. (1998) reported that the hercynite content of

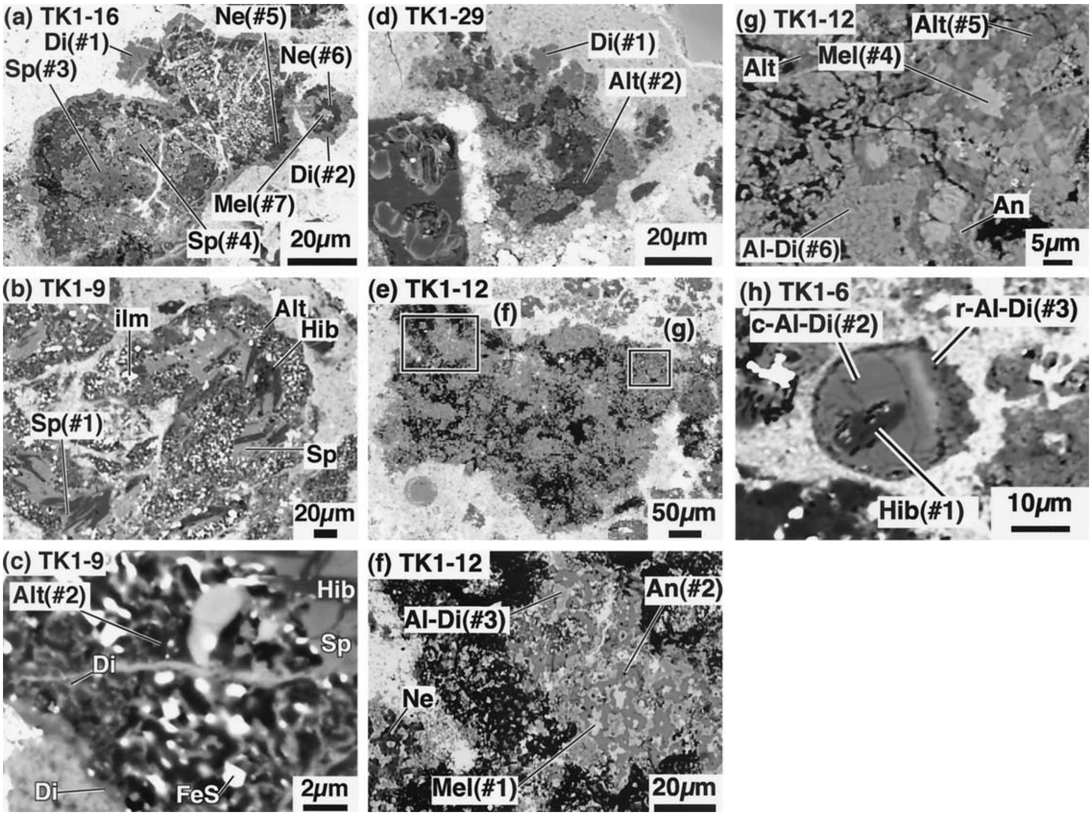

Fig. 3. Representative BSE images of FGIs in Kainsaz (TTK 1). The numbers in the figure indicate locations of chemical and O isotopic analyses reported in Table 2. Mineral abbreviations: Sp, spinel; An, anorthite; Di, diopside; Ne, nepheline; Mel, melilite; Hib, hibonite; Ilm, ilmenite; c-Al-Di, core of diopside; r-Al-Di, rim of Fe-Mg-Al-rich pyroxene. (a) Irregularly-shaped Sp-Alt-Px inclusion, TK1-16, 100 μm across. The CAI consists of aggregates of spinel grains with FeO zoning (average FeO = ~15 wt.%) enclosed by a nepheline layer. A rim of diopside encloses the CAI. TK1-16 is cut by many Fe-rich veins. (b) Irregularly-shaped Sp-Alt inclusion, TK1-9, 350 × 150 μm. (c) High magnification image of alteration layer of TK1-9. Small diopside particles (~2 μm) are scattered in the alteration layer. (d) Irregularly-shaped Px-Alt inclusion, TK1-29, 80 μm across. Alteration layer consists of a mixture of nepheline and unidentified Na-Al-Si-rich silicates. (e) Irregularly-shaped Mel-Alt-Px inclusion, TK1-12, 400 μm across. Alteration products are distributed heterogeneously in the CAI. (f) Primary mineral-rich area of TK1-12. Anorthite grains and Al-rich diopside enclose a core of melilite grains. (g) Alteration products-rich area of TK1-12. The area consists of a mixture of secondary minerals, anorthite and Al-rich diopside. The latter is partly converted to alteration products. (h) Rounded Hib-Px inclusion, TK1-6, 20 μm across.

spinel increases with increasing petrologic subtype in CO chondrites. In addition, hercynite contents of spinel are higher in FGIs without diopside rims (Fig. 3b; Table 2: hercynite mol.% = ~70 mol.%) than in those having diopside rims (Fig. 3a; Table 2: hercynite mol.% = ~30). These results suggest that the diopside rims inhibit Fe diffusion into FGIs and Fe diffusion generates high hercynite contents of spinel. It is plausible that Fe diffusion was caused by metamorphic processes in parent body (McSween, 1977a; Scott and Jones, 1990; Greenwood et al., 1992; Kojima et al., 1995; Russell et al., 1998). In spite of the large Fe-Mg exchanges, most spinel grains retain their original O-isotopic compositions ($\delta^{17,\ 18}$O= ~−40 to –50‰) (Fig. 7). The contrast in degree of exchange between Fe-Mg and O isotopes is consistent with the diffusivity contrast; Fe-Mg diffusion in spinel is about 10 orders of magnitude faster than that of oxygen self-diffusion (Ando and Ohishi, 1974; Freer and O'Reilly, 1980).

Petrography and O-isotopic characteristics indicate that melilite and anorthite in Kainsaz FGIs altered heterogeneously. On the other hand, O-isotopic compositions of spinel and diopside in the FGIs are almost always enriched in ^{16}O, indicating that these phases usually kept their pristine O-isotopic compositions despite aqueous alteration in the parent body. However, the spinel and diopside are expected to become ^{16}O-poor if aqueous alteration is very extensive. A heavily altered FGI contains spinel and diopside that appears to be altered in texture, chemical and O-isotopic compositions (Fig. 4 and Table 3). These results indicate the following alteration sequence of FGI spinel in CO chondrites: (1) Fe diffuses into spinel crystals by lattice diffusion mechanism; (2) aqueous fluid partially dissolves spinel and pyroxene, resulting in increasing porosity; (3) because the effective grain size becomes smaller, O self-diffusion leads to O-isotopic exchange; and (4) at the same time, recrystallization also enhances the O isotopic exchange.

Similar O isotopic exchange by aqueous alteration has been reported in olivine crystals of amoeboid olivine aggregates

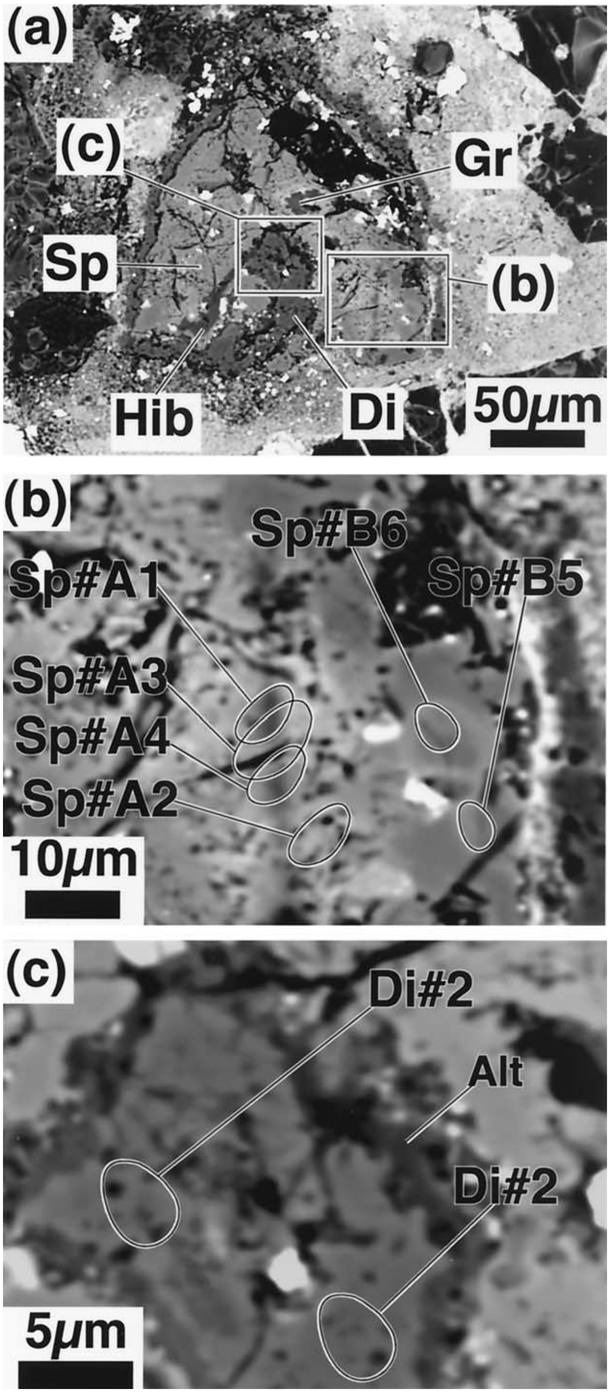

Fig. 4. BSE images of irregularly-shaped FGI, TK1–3. The numbers in the figure indicate locations of chemical and O-isotopic analyses reported in Table 3. (a) TK1-3 consists mainly of a spinel core with an incomplete diopside rim. Micrometer-sized patches of perovskite, hibonite and grossite grains exist in spinel core. Alteration products exist between the spinel and diopside rim. The alteration products contain sodium, potassium and sulfur. (b) Spinel in the core in TK1-3 has two different textures: one is porous (Sp#A), the other is smooth (Sp#B). The mean FeO content of Sp#A (~73 hercynite %) is higher than that of Sp#B (~56 hercynite %) (Table 3). (c) The diopside layer has a porous texture like Sp#A. The rim diopside is higher in FeO, Al_2O_3, TiO_2 and Cr_2O_3 than diopside in the core (Di#2; Table 3). Elliptical marks in figure denote SIMS analyses spots. Hib: hibonite. Gr: grossite. Alt: Na-S-K-Fe-rich unknown phases.

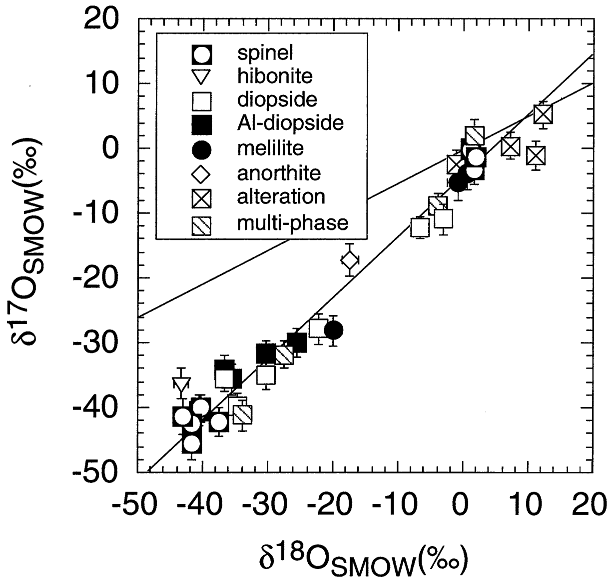

Fig. 5. Oxygen isotopic compositions of minerals from FGIs in TTK1 (Kainsaz). Analyses from all the FGI types of Kainsaz are plotted. Alteration denotes nepheline, graftonite, and unknown very fine-grained alteration minerals. Multi-phase is consistent with the overlap of data in Table 2.

(Imai and Yurimoto, 2003). Porous diopside grains are also observed in a rim of TK1-3. These results indicate that the alteration process is the same as in the case of spinel.

3.3. Primary Characteristics of CAIs in CO Chondrites

Clear evidence of chemical alteration of Yamato 81020 FGIs has not been observed. The FGIs seem to have preserved pristine O isotopic compositions, with $\delta^{17,\ 18}O$ = ~−40 to

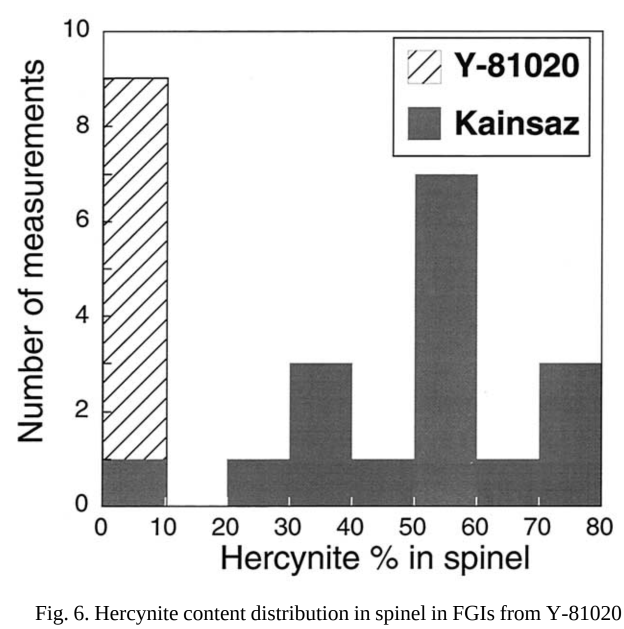

Fig. 6. Hercynite content distribution in spinel in FGIs from Y-81020 and Kainsaz.

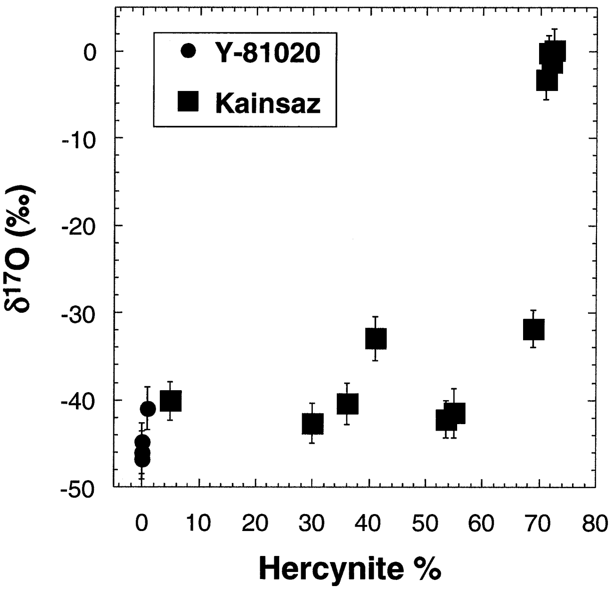

Fig. 7. Relationship between hercynite content and the ^{16}O-enrichment of FGI spinel from Y-81020 and TTK1. The ^{16}O-enrichment is nearly constant except for heavily altered inclusion TK1-3.

−50‰. Textures are consistent with formation of the FGIs by solid condensation from gas. Therefore, the FGIs seem to have condensed from ^{16}O-rich gas. However, we found one remarkable FGI with remelted texture (Y20-1). The O-isotopic composition of the igneous minerals (diopside and anorthite) is relatively depleted in ^{16}O ($\delta^{17,\ 18}$O = ~0 to −15‰), whereas relict spinel is enriched in ^{16}O ($\delta^{17,\ 18}$O = ~−40 to −50‰). These results indicate that the ^{16}O-rich precursor solids were partially melted and the O-isotopic compositions of the melt became ^{16}O-poor before solidification. Therefore, the remelting occurred in an ^{16}O-poor environment, which was different from the environment in which most Y-81020 FGIs formed. The existence of such an ^{16}O-isotope change in the solar nebula was proposed by Yurimoto et al. (2001).

4. CONCLUSIONS

Fine-grained CAIs from the Y-81020 CO3.0 chondrite are characterized by the absence of alteration textures, the presence of Mg-rich spinel and ^{16}O-rich mineral compositions. One exception with relatively ^{16}O-poor diopside and anorthite with distinct igneous textures was identified. In contrast, FGIs from Kainsaz (CO3.1–CO3.2) have Fe-rich spinel and abundant very fine-grained Na-rich phases that appear to have formed from alteration of melilite and anorthite. The Kainsaz FGIs show a mineral-dependent pattern of isotopic compositions with alteration products and melilite consistently depleted in ^{16}O relative to spinel, pyroxene and other primary phases.

These observations are interpreted to mean that: (1) all the primary phases of fine-grained CAIs in CO chondrites (hibonite, spinel, melilite, anorthite, Al-rich diopside, diopside and olivine) crystallized from ^{16}O-rich gas. (2) Some CAIs with igneous textures in CO3 chondrites formed by partial melting during reheating events in ^{16}O-poor gas in the solar nebula. (3) The CO3 chondrites, except for petrologic subtype 3.0, were subjected to parent-body metamorphism generating Fe-, Na-rich and ^{16}O-poor minerals in the CAIs. (4) Aqueous alteration on the parent body changed the O isotopic composition of all mineral species in CO3 fine-grained CAIs from ^{16}O-rich to ^{16}O-poor.

Acknowledgments—We appreciate M. Ito, T. Kunihiro and K. Nagashima for assistance with SIMS and useful support. We are grateful to J. T. Wasson, T. Fagan and H. Imai for useful and inspiring discussion. We thank T. Fagan, U. Ott, and an anonymous reviewer for improvement of English. We also thank Y. Lin, A. E. Rubin and an anonymous reviewer for their very helpful reviews and constructive comments. Finally we are grateful to U. Ott, associate editor, for constructive comments and suggestions. Supported by grants from Monbu-Kagaku-sho.

Associate editor: U. Ott

REFERENCES

Ando K. and Ohishi Y. (1974) Self-diffusion coefficients of oxygen ion in single crystals of $MgO \cdot nAl_2O_3$ spinels. *J. Chem. Phys.* **61**, 625–629.

Chizmadia L. J., Rubin A., and Wasson J. T. (2002) Mineralogy and petrology of amoeboid olivine inclusions in CO3 chondrites: Relationship to parent-body aqueous alteration. *Meteorit. Planet. Sci.* **37**, 1781–1796.

Clayton R. N. (1993) Oxygen isotopes in meteorites. *Ann. Rev. Earth Planet. Sci.* **21**, 115–149.

Clayton R. N. and Mayeda T. K. (1999) Oxygen isotope studies of carbonaceous chondrites. *Geochim. Cosmochim. Acta* **63**, 2089–2104.

Fagan T. J., McKeegan K. D., Krot A. N., and Keil K. (2001) Calcium-aluminum-rich inclusions in enstatite chondrites (II): Oxygen isotopes. *Meteorit. Planet. Sci.* **36**, 223–230.

Fagan T. J., Yurimoto H., Krot A. N., and Keil K. (2002) Constraints on oxygen isotopic evolution from an amoeboid olivine aggregate and Ca, Al-rich inclusion from the CV3 Efremovka [abstract]. *Lunar Planet. Sci.* **33,** #1507.

Freer R. and O'Reilly W. (1980) The diffusion of Fe^{2+} ions in spinels with relevance to the process of maghemitization. *Mineral. Mag.* **43**, 889–899.

Greenwood R. C., Hutchison R., Huss G. R., and Hutcheon I. D. (1992) CAIs in CO3 meteorites: Parent body or nebular alteration? [abstract]. *Meteoritics* **27**, 229.

Grossman J. N., Rubin A. E., Nagahara H., and King E. A. (1988) Properties of chondrules. In *Meteorites and the Early Solar System* (eds. J. F. Kerridge and M. S. Matthews), pp. 619–659. University of Arizona Press, Tucson.

Grossman L. (1972) Condensation in the primitive solar nebula. *Geochim. Cosmochim. Acta* **36**, 597–619.

Guan Y., McKeegan K. D., and MacPherson G. J. (2000) Oxygen isotopes in calcium-aluminum-rich inclusions from enstatite chondrites: New evidence for a single CAI source in the solar nebula. *Earth Planet. Sci. Lett.* **181**, 271–277.

Hashimoto A. and Grossman L. (1987) Alteration of Al-rich inclusions inside amoeboid olivine aggregates in the Allende meteorite. *Geochim. Cosmochim. Acta* **51**, 1685–1704.

Hiyagon H. and Hashimoto A. (1999) ^{16}O excesses in olivine inclusions in Yamato-86009 and Murchison Chondrites and their relation to CAIs. *Science* **283**, 828–831.

Huss G. R., Fahey A. J., Russell S. S., and Wasserburg G. J. (1995) Oxygen isotopes in refractory oxide minerals from primitive chondrites [abstract]. *Lunar Planet. Sci.* **26**, 641–642.

Imai H. and Yurimoto H. (2001) Two generations of olivine-growth in an amoeboid olivine aggregate from the Allende meteorite [abstract]. *Lunar Planet. Sci.* **32,** #1580.

Imai H. and Yurimoto H. (2003) Oxygen isotopic distribution in an amoeboid olivine aggregate from the Allende CV chondrite: Primary and secondary processes. *Geochim. Cosmochim. Acta* **67**, 765–772.

Ireland T. R., Fahey A. J., and Zinner E. K. (1991) Hibonite-bearing microspherules: A new type of refractory inclusions with large isotopic anomalies. *Geochim. Cosmochim. Acta* **55**, 367–379.

Itoh D. and Tomeoka K. (2003) Dark inclusions in CO3 chondrites: New indicators of parent-body processes. *Geochim. Cosmochim. Acta* **67**, 153–169.

Itoh S., Kojima H., and Yurimoto H. (2000) Petrography and oxygen isotope chemistry of calcium-aluminum rich inclusions in CO chondrites [abstract]. *Lunar Planet. Sci.* **31,** #1323.

Itoh S., Rubin A. E., Kojima H., Wasson J. T., and Yurimoto H. (2002) Amoeboid olivine aggregates and AOA-bearing chondrule from Y-81020 CO3.0 chondrite: Distributions of oxygen and magnesium isotopes [abstract]. *Lunar Planet. Sci.* **33,** #1490.

Kojima T., Yada S., and Tomeoka K. (1995) Ca-Al-inclusions in three Antarctic CO3 chondrites, YAMATO-81020, YAMATO-82050 and YAMATO-790992: Record of low-temperature alteration. *Proc. NIPR Symp. Antarct. Meteorite* **8**, 79–96.

Komatsu M., Krot A. N., Petaev M. I., Ulyanov A. A., Keil K., and Miyamoto M. (2001) Mineralogy and petrography of amoeboid olivine aggregates from the reduced CV3 chondrites Efremovka, Leoville and Vigarano: Products of nebular condensation, accretion and annealing. *Meteorit. Planet. Sci.* **36**, 629–641.

Kornacki A. S. and Wood J. A. (1984) Petrography and classification of Ca, Al-rich and olivine-rich inclusions in the Allende CV3 chondrite. *J. Geophys. Res.* **89,** *Suppl.*, B573–B587.

Krot A. N., McKeegan K. D., Russell S. S., Meibom A., Weisberg M. K., Zipfel J., Krot T. V., Fagan T. J., and Keil K. (2001) Refractory calcium-aluminum-rich inclusions and aluminum-diopside-rich chondrules in the metal-rich chondrites Hammadah al Hamra 237 and Queen Alexandra Range 94411. *Meteorit. Planet. Sci.* **36**, 1189–1216.

Krot A. N., Meibom A., Weisberg M. K., and Keil K. (2002) The CR chondrite clan. Implications for early solar system process. *Meteorit. Planet. Sci.* **37**, 1451–1490.

Lin Y. and Kimura M. (1998) Anorthite-spinel-rich inclusions in the Ningqiang carbonaceous chondrite: Genetic links with Type A and C inclusions. *Meteorit. Planet. Sci.* **33**, 435–446.

MacPherson G. J., Wark D. A., and Armstrong J. T. (1988) Primitive material surviving in chondrites: Refractory inclusions. In *Meteorites and the Early Solar System* (ed. M. S. Matthews), pp. 746–807. University of Arizona Press, Tucson.

McKeegan K. D., Leshin L. A., Russell S. S., and MacPherson G. J. (1998) Oxygen isotopic abundances in Calcium-Aluminum-rich inclusions from ordinary chondrites: Implications for nebular heterogeneity. *Science* **280**, 414–418.

McSween H. Y. (1977a) Carbonaceous chondrites of the Ornans type: A metamorphic sequence. *Geochim. Cosmochim. Acta* **41**, 477–491.

McSween H. Y. (1977b) Petrographic variations among carbonaceous chondrites of the Vigarano type. *Geochim. Cosmochim. Acta* **41**, 1777–1790.

Nomura K. and Miyamoto M. (1998) Hydrothermal experiments on alteration of Ca-Al-rich inclusions (CAIs) in carbonaceous chondrites: Implication for aqueous alteration in parent asteroids. *Geochim. Cosmochim. Acta* **62**, 3575–3588.

Russell S. S., Huss G. R., Fahey A. J., Greenwood R. C., Hutchison R., and Wasserburg G. J. (1998) An isotopic and petrologic study of calcium-aluminum-rich inclusions from CO3 meteorites. *Geochim. Cosmochim. Acta* **62**, 689–714.

Sahijpal S., McKeegan K. D., Krot A. N., Weber D., and Ulyanov A. A. (1999) Oxygen-isotopic compositions of calcium-aluminum-rich inclusions from the CH chondrites Acfer 182 and Patuxent Range 91546 [abstract]. *Meteorit. Planet. Sci.* **34**, A101.

Sakai T. and Yurimoto H. (1999) Oxygen isotope distribution in CAIs of the Murchison CM2 meteorite [abstract]. *Lunar Planet. Sci.* **30,** #1528.

Scott E. R. D. and Jones R. H. (1990) Disentangling nebular and asteroidal features of CO3 carbonaceous chondrite meteorites. *Geochim. Cosmochim. Acta* **54**, 2485–2502.

Sears D. W. G., Batchelor J. D., Lu J., and Keck B. D. (1991) Metamorphism of CO and CO-like chondrites and comparisons with type 3 ordinary chondrites. *Proc. NIPR Symp. Antarct. Meteorite* **4**, 319–343.

Shibata Y. (1996) Opaque minerals in Antarctic CO3 carbonaceous chondrites, Yamato-74135, -790992, -791717, -81020, -81025, -82050 and Allan Hills-77307. *Proc. NIPR Symp. Antarct. Meteorite* **9**, 79–96.

Simon S. B., Davis A. M., Grossman L., and Zinner E. K. (1998) Origin of hibonite-pyroxene spherules found in carbonaceous chondrites. *Meteorit. Planet. Sci.* **33**, 411–424.

Stolper E. (1982) Crystallization sequences of Ca-Al-rich inclusions from Allende: An experimental study. *Geochim. Cosmochim. Acta* **46**, 2159–2180.

Tomeoka K., Nomura K., and Takeda H. (1992) Na-bearing Ca-Al-rich inclusions in the Yamato791717 CO carbonaceous chondrite. *Meteoritics* **27**, 136–143.

Wark D. A. (1987) Plagioclase-rich inclusions in carbonaceous chondrite meteorites: Liquid condensates? *Geochim. Cosmochim. Acta* **51**, 221–242.

Wasson J. T., Yurimoto H., and Russell S. S. (2001) ^{16}O-rich melilite in CO3.0 chondrites. Possible formation of common, ^{16}O-poor melilite by aqueous alteration. *Geochim. Cosmochim. Acta* **65**, 4539–4549.

Yurimoto H., Ito M., and Nagasawa H. (1998) Oxygen isotope exchange between refractory inclusion in Allende and solar nebula gas. *Science* **282**, 1874–1877.

Yurimoto H., Asada Y., and Hirai K. (2001) Oxygen isotopic composition of fine-grained CAIs and genetic relation to coarse-grained CAIs [abstract]. *Meteorit. Planet. Sci.* **36**, A230.